Ceramics International 45 (2019) 4392–4397

Contents lists available at ScienceDirect

Ceramics International

journal homepage: www.elsevier.com/locate/ceramint

# Ultraviolet electroluminescence from nanostructural $SnO_2$-based heterojunction with high-pressure synthesized Li-doped ZnO as a hole source

Rui Deng[a,*], Jinliang Zhao[a], Duanyi Zhang[a], Jieming Qin[a,d,**], Bin Yao[b,c], Jing Song[a,e], Dayong Jiang[a], Yongfeng Li[b,c]

[a] School of Materials Science and Engineering, Changchun University of Science and Technology, Changchun 130022, PR China
[b] State Key Lab of Superhard Material, College of Physics, Jilin University, Changchun 130012, PR China
[c] Key Laboratory of Physics and Technology for Advanced Batteries (Ministry of Education), College of Physics, Jilin University, Changchun 130012, PR China
[d] School of Physics, Inner Mongolia University for Nationalities, Tongliao 028000, PR China
[e] State Key Laboratory of Applied Optics Changchun Institute of Optics, Fine Mechanics and Physics, Chinese Academy of Sciences, Changchun 130033, PR China

ARTICLE INFO

*Keywords:*
$SnO_2$
Nanobelt
Nanowire
Li-doped ZnO
High-temperature high-pressure method
Light-emitting diode

ABSTRACT

We report an ultraviolet (UV) electroluminescence (EL) in n-$SnO_2$/p-ZnO heterojunction light-emitting diodes with the nanostructural $SnO_2$ as an n-type layer and the Li-doped ZnO (ZnO:Li) synthesized by high-temperature high-pressure (HTHP) method as a high hole concentration p-type layer. Two kinds of $SnO_2$ nanostructures including nanobelts (NBs) and nanowires (NWs) were used to fabricate n-type layers in the heterojunctions. The two heterojunctions with different $SnO_2$ nanostructures demonstrate different light-emission feature in EL measurements. The $SnO_2$ NBs/p-ZnO heterojunction shows a blue emission band centered at 416 nm under forward-bias voltage. A strong UV emission peak located at 391 nm was observed for the $SnO_2$ NWs/p-ZnO heterojunction. Photoluminescence (PL) spectra indicate that the difference in EL is attributed to morphology-dependent light-emission feature in nanostructural $SnO_2$ layer. Our results suggest that the nanostructural $SnO_2$/ZnO:Li heterojunction is a potential and promising system in the UV optoelectronic field.

## 1. Introduction

Wide-bandgap oxides, as multifunctional semiconductor materials, have drawn much attention because of their potential applications in emerging semiconductor fields including transparent electronics, photovoltaic devices, photocatalysis, light-emitting diodes (LEDs), etc [1–4]. There are many excellent wide-bandgap oxide candidates involving ZnO, $In_2O_3$ and $SnO_2$ for ultraviolet (UV) optoelectronics application [5–10]. Among these candidates, $SnO_2$, as an n-type wide-bandgap semiconductor, has excellent chemical stability, high optical transparency and low electrical resistivity [11]. However, electron transition between conduction-band minimum (CBM) and valence-band maximum (VBM) is forbidden ("forbidden" bandgap) due to the symmetry of band structure of bulk $SnO_2$ although it has a direct bandgap. Therefore, intense band-edge UV emission from bulk $SnO_2$ is not expected. Nevertheless, it is recently reported that the "forbidden" bandgap in bulk $SnO_2$ can be allowed through nanoengineering and dopant engineering [12–15]. For example, $SnO_2$ nanostructures including quantum dots and nanowires demonstrated intense UV emission [15,16]. Thus, introducing nanostructure into $SnO_2$ is one of effective approaches to eliminate "forbidden" energy gap of $SnO_2$ and realize its band-edge UV emission. On the other hand, the lack of p-type $SnO_2$ is another obstacle to develop $SnO_2$-based LEDs. Differing from $SnO_2$ with the "forbidden" bandgap, ZnO usually can emit strong UV light owing to its large exciton binding energy. As the development of reliable p-type doping in ZnO, involving high-temperature high-pressure (HTHP) synthesis of p-type ZnO with hole-concentration [17], more optoelectronic devices based on p-type ZnO certainly emerge [18,19]. Therefore, it is expected that n-$SnO_2$/p-ZnO heterojunction with nanostructural active layer and high hole-concentration injection layer and could be a promising candidate for the UV photoelectronic application.

In this paper, to realize UV light emission, we designed and fabricated $SnO_2$/ZnO heterojunction LEDs based on $SnO_2$ nanostructures

* Corresponding author.
** Corresponding author at: School of Materials Science and Engineering, Changchun University of Science and Technology, Changchun 130022, PR China.
*E-mail addresses:* dengrui79@126.com (R. Deng), qjmqh@sohu.com (J. Qin).

https://doi.org/10.1016/j.ceramint.2018.11.114
Received 5 October 2018; Received in revised form 10 November 2018; Accepted 15 November 2018
Available online 16 November 2018

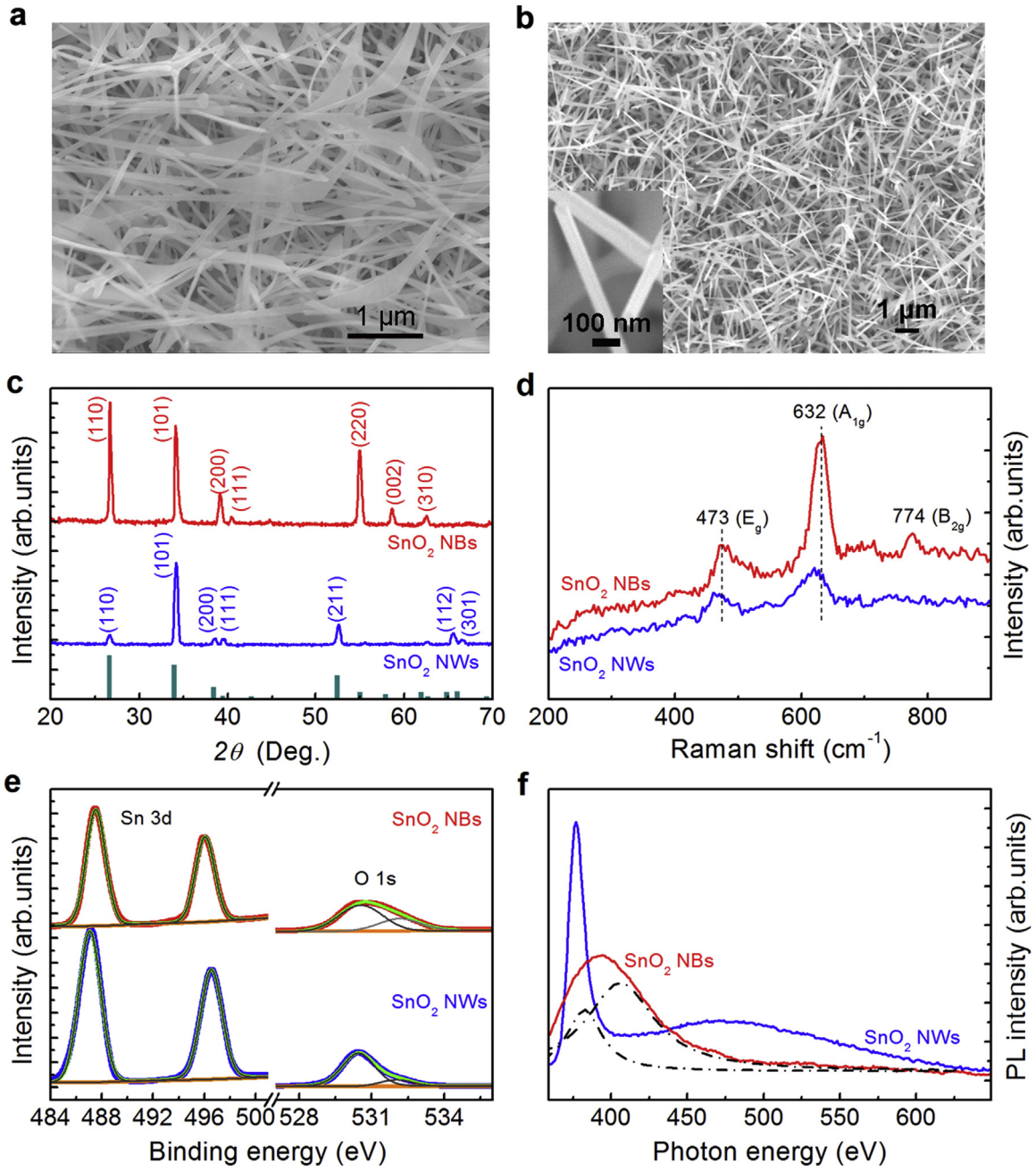


**Fig. 1.** Characterizations of the morphology, composition, structural and optical properties of the $SnO_2$ NBs and NWs. SEM images of $SnO_2$ products grown on Si substrates: (a) $SnO_2$ NBs and (b) $SnO_2$ NWs. The inset in (b) is the TEM image of a single $SnO_2$ NW. (c) XRD patterns, (d) Raman spectra, (e) XPS spectra and (f) RT PL spectra of the two $SnO_2$ samples.

and Li-doped ZnO. The intense UV EL emission from the nanostructural $SnO_2$ layer was observed. The HTHP-synthesized Li-doped p-type ZnO as a hole injection layer and the nanostructural $SnO_2$ with "allowed" bandgap play key roles in realizing UV emission.

## 2. Experimental process

The $SnO_2$ nanowires (NWs) and nanobelts (NBs) were synthesized on [111]- oriented silicon wafers using the vapor phase transport method under optimal growth conditions. High-purity $SnO_2$ (99.99%) and graphite (99.95%) powders with a mole ratio of 1:12.5 were uniformly mixed by ball milling method. The mixture was put into a quartz tube. The quartz tube was heated to 1050 °C in a tube furnace and kept for 60 min. A mixing gas with 100 SCCM flow of 99.5% Ar and 0.5% $O_2$ was employed as the carrier gas during the whole heating process. The gas pressure in the tube furnace was controlled at 7 mbar and 20 mbar for the $SnO_2$ NBs and NWs, respectively. When the growth process was completed, the products were naturally cooled down to room temperature. For the fabrication of Li-doped ZnO (ZnO:Li), a homogeneous mixture of ZnO and $Li_2O$ powder with a weight ratio of ZnO to $Li_2O$ of 52:1 was pressed into a circular slice. The slice was sintered at 1450 °C in a molybdenum ampoule under the pressure of 5 GPa and was kept for 15 min. After polishing both surface layers of the slice, the p-type ZnO:Li was obtained. When the preparation of the $SnO_2$ NBs, NWs and ZnO:Li were finished, an aluminum layer and Ni/Au were deposited onto the $SnO_2$ NWs (NBs) and ZnO:Li side as metal electrodes using a thermal evaporation method, respectively. Finally, the NWs (NBs) and ZnO:Li were bonded together using a clip to form the nanostructural

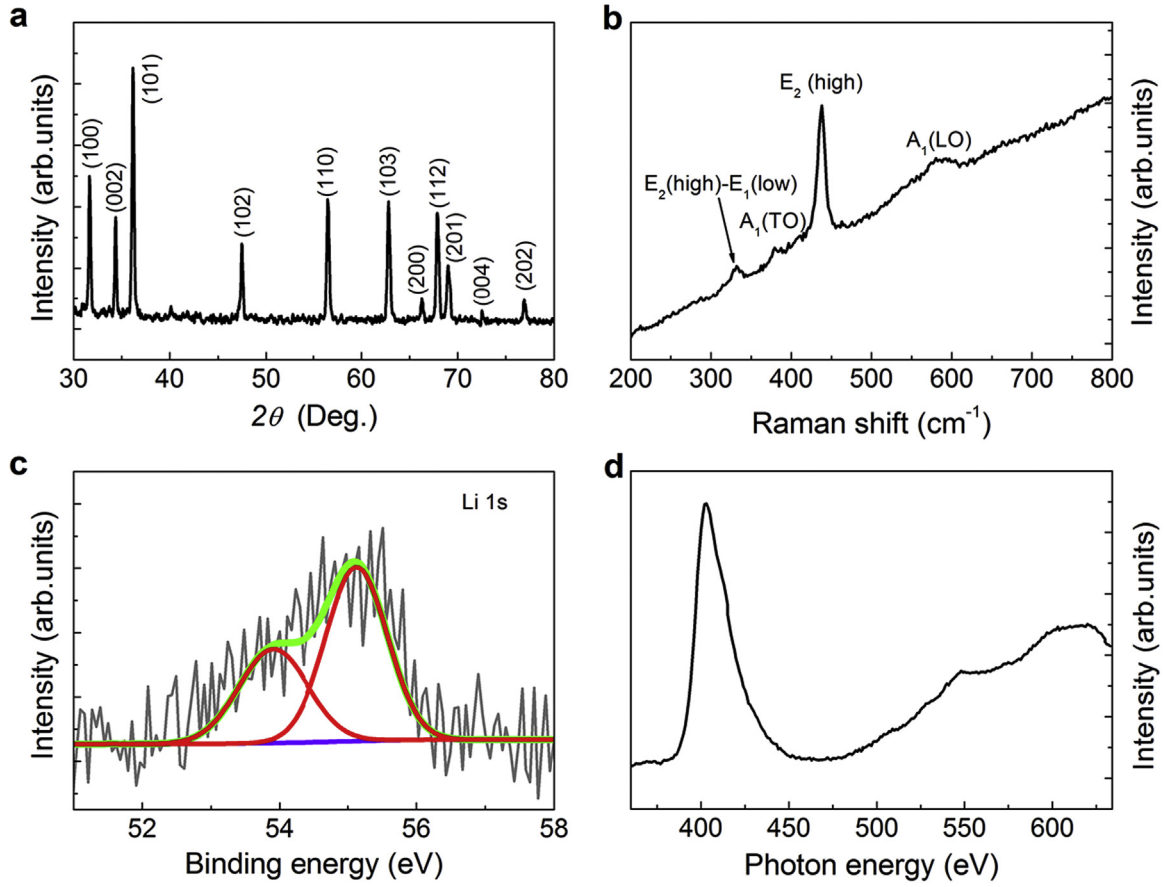


**Fig. 2.** Characterizations of the structural and optical properties of the ZnO:Li sample synthesized at high pressure: (a) XRD pattern; (b) Raman spectrum; (c) XPS of Li 1s and (d) RT PL spectrum.

$SnO_2$/ZnO:Li prototypical devices.

The crystal properties of the prepared ZnO and $SnO_2$ were measured by a Bruker D8 Advance powder x-ray diffractometer with Cu Kα radiation of λ = 1.5406 Å. The morphologies of the prepared ZnO and $SnO_2$ were recorded by a Hitachi S4800 field-emission scanning electron microscope (FESEM). Raman and photoluminescence (PL) spectra of the samples were characterized by a 325-nm line He-Cd laser. X-ray photoelectron spectroscopy (XPS) was used to detect the composition and chemical state of Sn, O and Li. All XPS data were calibrated via correcting the C 1s peak to 284.6 eV. The current-voltage (I-V) curves of the $SnO_2$ NWs (NBs)/ZnO:Li heterojunctions were recorded using a semiconductor characterization system (Keithley 4200). Electroluminescence (EL) spectra were recorded in a spectrometer using a current source to excite devices.

## 3. Results and discussion

### 3.1. Morphology, structure, composition and optical properties of $SnO_2$ NBs and NWs

The morphologies of the as-synthesized $SnO_2$ NBs and NWs are displayed in Fig. 1a and b, respectively. The $SnO_2$ NBs sample consists of a large quality of ribbon-like structures. The length of nanobelts are in range of several to more than dozen micrometers. The width, measured between the two long sides of nanobelts, are 40–400 nm, while the thickness is 50–60 nm. The average diameter for the $SnO_2$ NWs is about ~ 60 nm. An enlarged image of the individual nanowire is shown in the inset of Fig. 1b. The smooth surface can be observed. It is worth noting that the morphology, shape and size of $SnO_2$ nanostructures are strongly dependent upon the growth pressure [20]. Shi et al. proposed a boundary layer theory to interpret the morphology evolution with growth pressure [21], which involves the pressure-dependent diffusivity of reactant atoms onto the product surface.

The XRD patterns of the $SnO_2$ NBs and NWs are shown in Fig. 1c. All diffraction peaks are derived from the diffraction of $SnO_2$ with rutile structure, in agreement with the standard XRD pattern (PDF #880287). There is no secondary phase in the XRD patterns, indicating that both $SnO_2$ NBs and NWs are single phase. In order to further confirm the crystalline properties of $SnO_2$ NBs and NWs, we performed Raman spectroscopy measurements. It can be found from Fig. 1d that, three strong Raman peaks are assigned to $E_g$, $A_{1g}$ and $B_{2g}$ modes of rutile $SnO_2$. This result indicates that the $SnO_2$ NWs and NBs are single phase and in accordance with the XRD patterns. The mode $A_{1g}$ peaks are found at 632 and 622 $cm^{-1}$ for the $SnO_2$ NBs and NWs, respectively, which are lower than that of bulk $SnO_2$ of 638 $cm^{-1}$. It was reported that the $A_{1g}$ mode is associated to the size of $SnO_2$. When the size of nanostructural $SnO_2$ decreases, the $A_{1g}$ mode moves to the lower wavenumber [22,23]. Therefore, the shift of $A_{1g}$ mode towards to low wavenumber with respect to bulk $SnO_2$ is ascribed to quantum size effect.

Fig. 1e shows the XPS spectra of Sn 3d and O 1s states for the $SnO_2$ NBs and NWs. The Sn $3d_{5/2}$ peaks of the $SnO_2$ NBs and NWs are located at around 487.5 eV and 487.1 eV, respectively, indicating the $Sn^{4+}$ in the $SnO_2$[24]. The Sn $3d_{5/2}$ peak of NBs shows a shift to a higher binding energy with respect to the NWs, which is due to higher concentration of oxygen vacancy ($V_O$) in $SnO_2$ NBs [24]. For both samples, it is observed that an asymmetric peak shape with a main peak and a shoulder in the spectra of O 1s, suggesting that oxygen is composed of different states. To further study the possible states of oxygen, we performed the peak fitting using Voigt line shape with a Shirley

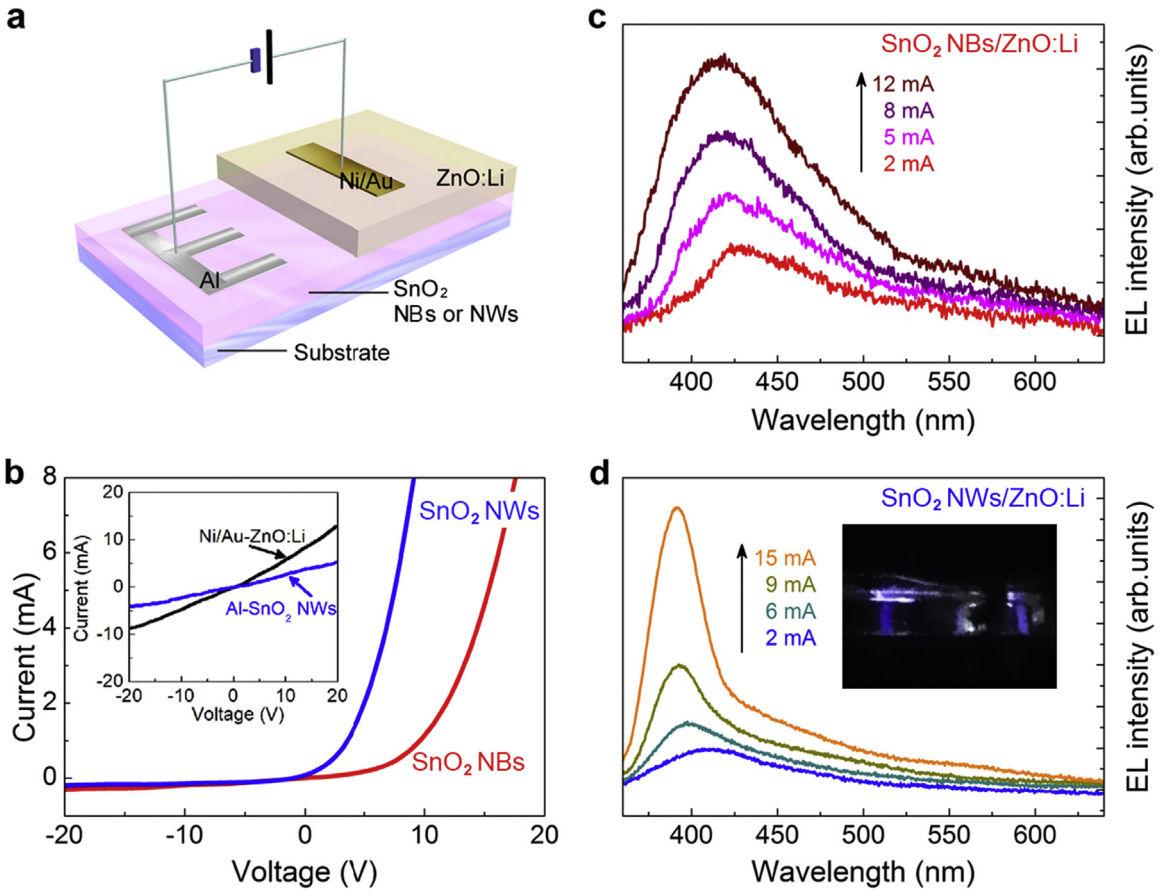


**Fig. 3.** Device structure and performances of the n-$SnO_2$ NBs /p-ZnO:Li and n-$SnO_2$ NWs/p-ZnO:Li heterojunction LEDs. (a) Schematic illustration of the $SnO_2$ NBs (or NWs)/p:ZnO:Li heterojunction. (b) I-V curves of the n-$SnO_2$ NBs/p-ZnO:Li and n-$SnO_2$ NWs/p-ZnO:Li. The inset in (b) shows the I-V curves with Ohmic contacts between two Al electrodes on the $SnO_2$ NWs as well as between two Ni/Au electrodes on the p-ZnO:Li. EL spectra of the (c) n-$SnO_2$ NBs/p-ZnO:Li and (d) n-$SnO_2$ NWs/p-ZnO:Li heterojunctions. The inset in (d) shows the photograph of the n-$SnO_2$ NWs/p-ZnO:Li heterojunction LED biased under a forward current.

background. The two fitting subpeaks are at 530.5 and 532.1 eV, respectively. The main peak at 530.5 eV is due to the oxygen in the lattice of rutile $SnO_2$. The shoulder located at 532.1 eV is ascribed to the $V_O$ on the surface of nanostructural $SnO_2$ [25,26]. The relative intensity of the shoulder to the main peak for the $SnO_2$ NBs is stronger than that for the $SnO_2$ NWs, suggesting higher concentration of $V_O$ on the surface of the $SnO_2$ NBs. Therefore, the different growth pressure can lead to the difference in $V_O$ concentration of the nanostructural $SnO_2$.

To study the luminescent properties of $SnO_2$ NWs and NBs, PL characterization was carried out. Fig. 1f illustrates the PL spectra of $SnO_2$ NWs and NBs recorded at room temperature. For the $SnO_2$ NWs, it is observed that a strong and sharp UV light emission peak centered at 378 nm (3.28 eV in photon energy) and a weak visible light emission band located at 481 nm (2.58 eV). For the $SnO_2$ NBs, there is a broad emission band in the violet and UV region. The broad PL emission band for the $SnO_2$ NBs can be fitted into two emission peaks centered at 382 nm (photon energy of 3.25 eV) and 406 nm (3.05 eV), respectively. The emission at ~ 380 nm from the $SnO_2$ NWs and NBs has the same derivation, which is attributed to the band-edge recombination of conduction-band (CB) to acceptors (eA°) and excitons binding at neutral donors (D°X) [16,27,28]. The blue emission peak of the $SnO_2$ NBs located at 406 nm is related to the oxygen vacancies ($V_O$) on the surface [24], which agrees with the XPS result. The observation of UV emission peaks for both nanostructural $SnO_2$ indicate that the band edge dipole-forbidden rule of bulk $SnO_2$ is broken. The surface defect states play key role in inducing direct gap transitions and generating possible luminescence [29–31]. Compared with the $SnO_2$ NBs, the $SnO_2$ NWs exhibit a higher UV luminescence quality, which lays a solid ground for the application of intense UV emission.

### 3.2. Structure, composition and optical properties of ZnO:Li synthesized using high pressure method

The XRD pattern of the ZnO:Li synthesized by HTHP method is exhibited in Fig. 2a. All diffraction peaks are ascribed to the hexagonal ZnO with the wurtzite structure and no impurity phase is detected. The strong diffraction peaks indicate that the ZnO:Li is well crystallized. To further confirm the structure of ZnO:Li, we recorded Raman spectrum of the ZnO:Li, as shown in Fig. 2b. There are four Raman peaks at 331, 379, 437, and 578 $cm^{-1}$, which are attributed to $E_2^{high}$-$E_2^{low}$, $A_1^{TO}$, $E_2^{high}$ and $A_1^{LO}$ modes of wurtzite ZnO [32–35], respectively.

Fig. 2c shows the Li 1s XPS spectrum of the Li-doped ZnO. There is an asymmetry peak with a weak shoulder, which is fitted by two subpeaks located at 53.9 and 55.1 eV, respectively. The peak and shoulder located at 55.1 eV and 53.9 eV are attributed to Li substituting Zn ($Li_{Zn}$) and interstitial Li ($L_i$) [36], respectively, indicating that the Li impurities are doped into ZnO lattice.

The representative PL spectrum of the ZnO:Li measured at room temperature is shown in Fig. 2d. The spectrum consists of a UV-violet light emission peak centered at ~ 402 nm (3.08 eV) and a broad visible light emission band related to deep-level (DL) [37–39]. The strong UV-violet emission peak is attributed to electron transition from CB to acceptor defect of Zn vacancy ($V_{Zn}$) which is introduced by Li doping [40,41].

### 3.3. Performance of $SnO_2$ NWs (NBs)/ZnO:Li heterojunction LEDs

We fabricated two LEDs with $SnO_2$ NWs/ZnO:Li and $SnO_2$ NBs/ZnO:Li heterojunctions. The $SnO_2$ NWs (NBs) and ZnO:Li were bonded together by a binder clip to form $SnO_2$/ZnO heterojunction devices. The Al and Ni/Au were used as the device electrodes of $SnO_2$ and ZnO sides, respectively. Fig. 3a shows the schematic of the device structure of LED. We first recorded the *I-V* curves of the two devices, as shown in Fig. 3b. The *I-V* curve exhibits a p-n junction rectifying behavior for both devices. The inset of Fig. 3b shows the *I-V* curves between two separated Al electrodes on the $SnO_2$ NWs as well as between two Ni/Au electrodes on the p-ZnO: Li. The linear relationship exhibits the good Ohmic contacts for metal electrode and oxides, implying that the rectifying behavior originates from the p–njunction instead of the Schottky contacts. The current of $SnO_2$ NWs/ZnO:Li heterojuction is much larger than that of the $SnO_2$ NBs/ZnO:Li at an identical forward voltage. The turn-on voltage of the $SnO_2$ NWs/ZnO:Li heterojunction is determined to be ~ 2.6 V. The voltage value is approximate three times lower than that (~ 9 V) of the $SnO_2$ NBs heterojunction device. The difference in *I-V* curves for both devices is due to the different contact area between $SnO_2$ NWs (NBs) and the electrodes, which is similar to the previous results reported by Ref.[41]. The contact area of $SnO_2$ NWs to electrode is smaller than that of $SnO_2$ NBs counterpart. The electric field across the device enhances as applying the same voltage on the electrode with small contact area, which increases the current and lowers the turn-on voltage and the leakage current [42].

Figs. 3c and 3d show the EL spectra of the two LEDs with $SnO_2$ NBs/ZnO:Li and $SnO_2$ NWs/ZnO:Li heterojunctions, respectively. It is observed that a broad-band blue-light emission with the center at ~ 420 nm for the $SnO_2$ NBs/ZnO:Li heterojunction. Differing from the $SnO_2$ NBs/ZnO:Li heterojunction, a rather narrow UV-violet emission peak is demonstrated for the NWs/ZnO:Li heterojunction. The inset in Fig. 3d shows the photograph of $SnO_2$ NWs/ZnO:Li heterojunction under the forward current, capturing the violet light. Under the injection current of 15 mA, the emission peak is located at 391 nm and its full width at half maximum (FWHM) is ~ 24 nm. It should be noted that the emission peak in the PL of $SnO_2$ NWs is located at 37 nm and close to the EL peak position. Thus, when a forward bias is applied on the LED, the radiative recombination happens in the $SnO_2$ NWs side (as an active layer) where the electrons recombine with the holes injected from the p-type ZnO:Li layer. However, the blue emission band in EL spectra of NBs/ZnO:Li heterojunction is ascribed from radiative recombination processing on both sides of the heterojunction by the comparsion of the EL spectra with PL ones of $SnO_2$ NBs and ZnO: Li.

## 4. Conclusions

In summary, the $SnO_2$ NWs (and NBs)/ZnO:Li heterojunction LEDs with high-pressure synthetized ZnO:Li as a hole source were fabricated. The $SnO_2$ NWs/ZnO:Li heterojunction exhibits the UV emission under the forward voltage. The UV emission peak is ascribed to that the radiative recombination between injected holes from ZnO:Li side and the electrons in the $SnO_2$ side. Our results may provide a route to find some potential applications of ZnO/$SnO_2$ heterojunction in the future display and solid-state lighting devices.

## Acknowledgement

This work is supported by the National Natural Science Foundation of China under Grant Nos. 10874178, 11074093, 61205038, 11464035 and 11274135, Specialized Research Fund for the Doctoral Program of Higher Education under Grant No. 20130061130011, Ph.D. Programs Foundation of Ministry of Education of China under Grant No. 20120061120011, Natural Science Foundation of Jilin Province under grant No. 201115013. The Science and Technology Development Project of Jilin Province under grant No. 20170101142JC, 20140101052JC. Project funded by China Postdoctoral Science Foundation 2017M611287. Scientific and Technological “13th Five-Year Plan” Project of Jilin Provincial Department of Education Grant No. JJKH20170610KJ. This work was also supported by High Performance Computing Center of Jilin University, China.

## References

[1] L. Liu, Z. Liu, Y. Yang, M. Geng, Y. Zou, M.B. Shahzad, Y. Dai, Y. Qi, Photocatalytic properties of Fe-doped ZnO electrospun nanofibers, Ceram. Int. 44 (16) (2018) 19998–20005.
[2] E. Mendoza-Mendoza, A.G. Nuñez-Briones, L.A. García-Cerda, R.D. Peralta-Rodríguez, A.J. Montes-Luna, One-step synthesis of ZnO and Ag/ZnO heterostructures and their photocatalytic activity, Ceram. Int. 44 (6) (2018) 6176–6180.
[3] N. Ahmad, S. Khan, M.M.N. Ansari, Optical, dielectric and magnetic properties of Mn doped SnO2 diluted magnetic semiconductors, Ceram. Int. 44 (13) (2018) 15972–15980.
[4] M.-T. Tsai, Y.-S. Chang, Y.-C. Liu, Photocatalysis and luminescence properties of zinc stannate oxides, Ceram. Int. 43 (2017) S428–S434.
[5] E. Comini, G. Faglia, G. Sberveglieri, Z. Pan, Z.L. Wang, Stable and highly sensitive gas sensors based on semiconducting oxide nanobelts, Appl. Phys. Lett. 81 (10) (2002) 1869–1871.
[6] C. Li, D. Zhang, X. Liu, S. Han, T. Tang, J. Han, C. Zhou, In2O3 nanowires as chemical sensors, Appl. Phys. Lett. 82 (10) (2003) 1613–1615.
[7] Z.L. Wang, J. Song, Piezoelectric nanogenerators based on zinc oxide nanowire arrays, Science 312 (5771) (2006) 242–246.
[8] M.N. Rezaie, N. Manavizadeh, F.D. Nayeri, M.M. Bidgoli, E. Nadimi, F.A. Boroumand, Effect of seed layers on low-temperature, chemical bath deposited ZnO nanorods-based near UV-OLED performance, Ceram. Int. 44 (5) (2018) 4937–4945.
[9] R. Yousefi, F. Jamali-Sheini, A. Khorsand Zak, M. Azarang, Growth and optical properties of ZnO–In2O3 heterostructure nanowires, Ceram. Int. 39 (5) (2013) 5191–5196.
[10] B.M.M. Faustino, P.J.S. Foot, R.A. Kresinski, Synthesis and photoluminescent properties of Sm3+-doped SnO2 nanoparticles, Ceram. Int. 42 (16) (2016) 18474–18478.
[11] M. Batzill, U. Diebold, The surface and materials science of tin oxide, Prog. Surf. Sci. 79 (2) (2005) 47–154.
[12] H. Zhou, R. Deng, Y.-F. Li, B. Yao, Z.-H. Ding, Q.-X. Wang, Y. Han, T. Wu, L. Liu, Wavelength-tuned light emission via modifying the band edge symmetry: doped SnO2 as an example, J. Phys. Chem. C 118 (12) (2014) 6365–6371.
[13] S. Zhou, L. Li, Y. Yuan, A.W. Rushforth, L. Chen, Y. Wang, R. Böttger, R. Heller, J. Zhao, K.W. Edmonds, R.P. Campion, B.L. Gallagher, C. Timm, M. Helm, Precise tuning of the Curie temperature of (Ga,Mn)As-based magnetic semiconductors by hole compensation: support for valence-band ferromagnetism, Phys. Rev. B 94 (7) (2016) 075205.
[14] Y. Huang, Y. Li, R. Deng, B. Yao, Z. Ding, L. Zhang, H. Zhao, Z. Zhang, L. Liu, Y. Sui, Highly spectrum-selective near-band-edge ultraviolet photodiode based on indium oxide with dipole-forbidden bandgap transition, Ceram. Int. 42 (7) (2016) 8017–8021.
[15] Y. Huang, Y. Li, B. Yao, Z. Ding, R. Deng, L. Zhang, H. Zhao, A facile route to realize ultraviolet emission in a nano-engineered SnO2-based light-emitting diode, J. Phys. D: Appl. Phys. 48 (46) (2015) 465103.
[16] B. Liu, C.W. Cheng, R. Chen, Z.X. Shen, H.J. Fan, H.D. Sun, Fine structure of ultraviolet photoluminescence of tin oxide nanowires, J. Phys. Chem. C 114 (8) (2010) 3407–3410.
[17] J.M. Qin, B. Yao, Y. Yan, J.Y. Zhang, X.P. Jia, Z.Z. Zhang, B.H. Li, C.X. Shan, D.Z. Shen, Formation of stable and reproducible low resistivity and high carrier concentration p-type ZnO doped at high pressure with Sb, Appl. Phys. Lett. 95 (2) (2009) 022101.
[18] S. Chu, G. Wang, W. Zhou, Y. Lin, L. Chernyak, J. Zhao, J. Kong, L. Li, J. Ren, J. Liu, Electrically pumped waveguide lasing from ZnO nanowires, Nat. Nano 6 (8) (2011) 506–510.
[19] X. Yang, C.-X. Shan, M.-M. Jiang, J.-M. Qin, G.-C. Hu, S.-P. Wang, H.-A. Ma, X.-P. Jia, D.-Z. Shen, Intense electroluminescence from ZnO nanowires, J. Mater. Chem. C 3 (20) (2015) 5292–5296.
[20] S. Das, V. Jayaraman, SnO2: a comprehensive review on structures and gas sensors, Prog. Mater. Sci. 66 (2014) 112–255.
[21] Z.-F. Shi, Y.-T. Zhang, X.-J. Cui, S.-W. Zhuang, B. Wu, J.-Y. Jiang, X.-W. Chu, X. Dong, B.-L. Zhang, G.-T. Du, Epitaxial growth of vertically aligned ZnO nanowires for bidirectional direct-current driven light-emitting diodes applications, CrystEngComm 17 (1) (2015) 40–49.
[22] A.F. Khan, M. Mehmood, M. Aslam, M. Ashraf, Characteristics of electron beam evaporated nanocrystalline SnO2 thin films annealed in air, Appl. Surf. Sci. 256 (7) (2010) 2252–2258.
[23] C.C. Yang, S. Li, Size-Dependent Raman Red Shifts of Semiconductor Nanocrystals, J. Phys. Chem. B 112 (45) (2008) 14193–14197.
[24] Y. Yang, Y. Wang, S. Yin, Oxygen vacancies confined in SnO2 nanoparticles for desirable electronic structure and enhanced visible light photocatalytic activity, Appl. Surf. Sci. 420 (2017) 399–406.
[25] J. Dai, C. Xu, J. Guo, X. Xu, G. Zhu, Y. Lin, Brush-like SnO2/ZnO hierarchical nanostructure: Synthesis, characterization and application in UV photoresponse, AIP Adv. 3 (6) (2013) 062108.

[26] L.Z. Liu, X.L. Wu, J.Q. Xu, T.H. Li, J.C. Shen, P.K. Chu, Oxygen-vacancy and depth-dependent violet double-peak photoluminescence from ultrathin cuboid SnO2 nanocrystals, Appl. Phys. Lett. 100 (12) (2012) 121903.
[27] R. Chen, G.Z. Xing, J. Gao, Z. Zhang, T. Wu, H.D. Sun, Characteristics of ultraviolet photoluminescence from high quality tin oxide nanowires, Appl. Phys. Lett. 95 (6) (2009) 061908.
[28] H.Y. Yang, S.F. Yu, S.P. Lau, S.H. Tsang, G.Z. Xing, T. Wu, Ultraviolet coherent random lasing in randomly assembled SnO2 nanowires, Appl. Phys. Lett. 94 (24) (2009) 241121.
[29] A. Kar, M.A. Stroscio, M. Dutta, J. Kumari, M. Meyyappan, Observation of ultraviolet emission and effect of surface states on the luminescence from tin oxide nanowires, Appl. Phys. Lett. 94 (10) (2009) 101905.
[30] M. Gaidi, A. Hajjaji, R. Smirani, B. Bessais, M.A.E. Khakani, Structure and photoluminescence of ultrathin films of SnO2 nanoparticles synthesized by means of pulsed laser deposition, J. Appl. Phys. 108 (6) (2010) 063537.
[31] S. Das, S. Kar, S. Chaudhuri, Optical properties of SnO2 nanoparticles and nanorods synthesized by solvothermal process, J. Appl. Phys. 99 (11) (2006) 114303.
[32] M. Tzolov, N. Tzenov, D. Dimova-Malinovska, M. Kalitzova, C. Pizzuto, G. Vitali, G. Zollo, I. Ivanov, Vibrational properties and structure of undoped and Al-doped ZnO films deposited by RF magnetron sputtering, Thin Solid Films 379 (1–2) (2000) 28–36.
[33] T.C. Damen, S.P.S. Porto, B. Tell, Raman effect in zinc oxide, Phys. Rev. 142 (2) (1966) 570–574.
[34] E.V. Vilejshikova, P.A. Loiko, G.E. Rachkovskay, G.B. Zakharevich, K.V. Yumashev, Up-conversion luminescence in oxyfluoride glass-ceramics with PbF2:(Yb3+, Eu3+, RE3+) (RE = Tm, Ho, OR Er) nanocrystals, J. Appl. Spectrosc. 83 (5) (2016) 723–729.
[35] A.E. Manouni, F.J. Manjón, M. Mollar, B. Marí, R. Gómez, M.C. López, J.R. Ramos-Barrado, Effect of aluminium doping on zinc oxide thin films grown by spray pyrolysis, Superlattices Microstruct. 39 (1–4) (2006) 185–192.
[36] J.B. Yi, C.C. Lim, G.Z. Xing, H.M. Fan, L.H. Van, S.L. Huang, K.S. Yang, X.L. Huang, X.B. Qin, B.Y. Wang, T. Wu, L. Wang, H.T. Zhang, X.Y. Gao, T. Liu, A.T.S. Wee, Y.P. Feng, J. Ding, Ferromagnetism in dilute magnetic semiconductors through defect engineering: li-doped ZnO, Phys. Rev. Lett. 104 (13) (2010) 137201.
[37] B. Lin, Z. Fu, Y. Jia, Green luminescent center in undoped zinc oxide films deposited on silicon substrates, Appl. Phys. Lett. 79 (7) (2001) 943–945.
[38] G.W. Tomlins, J.L. Routbort, T.O. Mason, Zinc self-diffusion, electrical properties, and defect structure of undoped, single crystal zinc oxide, J. Appl. Phys. 87 (1) (2000) 117–123.
[39] S.B. Zhang, S.H. Wei, A. Zunger, Intrinsicn-type versusp-type doping asymmetry and the defect physics of ZnO, Phys. Rev. B 63 (7) (2001).
[40] N. Bagheri, M.H.M. Ara, N. Ghazyani, Characterization and doping effects study of high hole concentration Li-doped ZnO thin film prepared by sol–gel method, J. Mater. Sci.: Mater. Electron. 27 (2) (2016) 1293–1298.
[41] T.P. Rao, M.C.S. Kumar, Realization of stable p-type ZnO thin films using Li–N dual acceptors, J. Alloy. Compd. 509 (35) (2011) 8676–8682.
[42] Y.-P. Hsieh, H.-Y. Chen, M.-Z. Lin, S.-C. Shiu, M. Hofmann, M.-Y. Chern, X. Jia, Y.-J. Yang, H.-J. Chang, H.-M. Huang, S.-C. Tseng, L.-C. Chen, K.-H. Chen, C.-F. Lin, C.-T. Liang, Y.-F. Chen, Electroluminescence from ZnO/Si-nanotips light-emitting diodes, Nano Lett. 9 (5) (2009) 1839–1843.